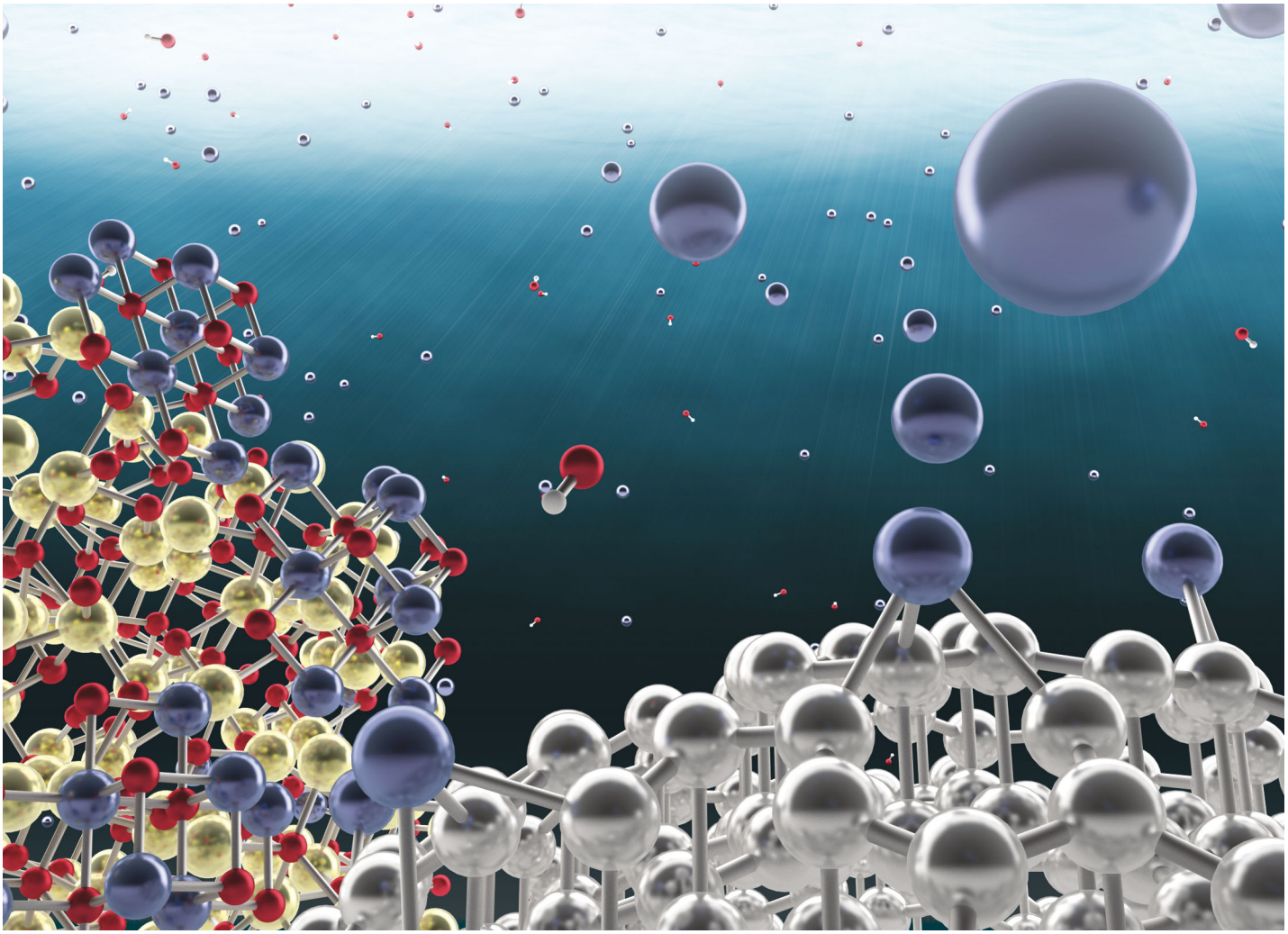

Showcasing research from the Laboratory of Energy Storage and Conversion and the Laboratory for Nanobioelectronics at the NanoEngineering Department of the University of California, San Diego, USA

Title: Deposition of ZnO on bismuth species towards a rechargeable Zn-based aqueous battery

This paper reports the recharge mechanism of Zn-based batteries. The systematic Bi_2O_3 composite additive study involving electrochemistry, microscopy, and spectroscopy has revealed the key mechanism after the discharge process. Without the Bi_2O_3 additive, upon discharge or oxidation, zincate ions are formed and dissolve into electrolyte. With the Bi_2O_3 additive, upon oxidation, zincate ions are formed and relaxed into ZnO on the surface of the bismuth species. Since zincate ions stay on the electrode, the cycle life of the Zn-based battery is prolonged. This mechanism paves the way for further prolonging the cycle life of Zn-based batteries and possibly other conversion type batteries.

As featured in:

See Joseph Wang, Y. Shirley Meng *et al.*, *Phys. Chem. Chem. Phys.*, 2016, **18**, 26376.

ROYAL SOCIETY OF CHEMISTRY

www.rsc.org/pccp

Registered charity number: 207890

PCCP

PAPER

View Article Online
View Journal | View Issue

Cite this: *Phys. Chem. Chem. Phys.*, 2016, **18**, 26376

Deposition of ZnO on bismuth species towards a rechargeable Zn-based aqueous battery†

JaeWook Shin,‡ Jung-Min You,‡ Jungwoo Z. Lee, Rajan Kumar, Lu Yin, Joseph Wang* and Y. Shirley Meng*

Received 29th June 2016,
Accepted 10th August 2016

DOI: 10.1039/c6cp04566a

www.rsc.org/pccp

Zn aqueous batteries typically suffer from poor cycle life because water soluble zincate ions are formed during the oxidation of Zn. When Zn is oxidized, most of the Zn^{2+} ions detach from the current collector and become electrochemically inactive, leaving the battery non-rechargeable. Numerous reports demonstrate the use of Bi_2O_3 as an electrode additive to enhance electrochemical performance and they attribute this phenomenon to the improvement in electrical conductivity. However, conductivity does not have an effect on the intrinsic solubility of the zincate ion. We conduct a series of characterizations to provide a comprehensive mechanistic role of Bi_2O_3 in the Zn electrode. We find that upon oxidation, zincate ions are formed but they relax into ZnO on the surface of the bismuth species. This work proposes that the reason for the prolonged cycle life is due to the deposition of ZnO through relaxation and this prevents losing electrochemically active materials. This finding paves the way for further improving the cycle life and understanding the mechanism of the Zn based rechargeable aqueous batteries and possibly other conversion types of rechargeable batteries.

1. Introduction

Rechargeable or secondary batteries have become an essential part of everyday life. A battery is the most efficient way of storing energy because it does not need an external conversion mechanism.[1] While the need for a low-cost battery is rising, lithium-ion batteries (LIBs) dominate the secondary battery in the market even though the material synthesis for a LIB is energy intensive and expensive.[2–5] LIBs utilize ceramic oxides and highly ordered graphite, which require high temperature synthesis and organic electrolytes, which are flammable and require expensive casing. One attractive option to lower the cost of energy storage is to design secondary batteries with aqueous electrolytes. Zn anodes are a promising aqueous battery material because they are a nontoxic, earth abundant, low-cost, and energy dense resource.[6] Utilizing the Zn anode also raises the working voltage due to its low reduction voltage; thus applying a rechargeable Zn anode can lead to a dramatic drop in the cost of secondary batteries.[7]

Zn anodes are one of the oldest electrochemical electrodes dating back to the batteries invented by Alessandro Volta in the 1800s, yet commercially rechargeable Zn anode implementation is scarce because the Zn anode suffers from a critical intrinsic issue. It has long been discovered that when Zn oxidizes (or discharges), zincate ions are formed and relax into ZnO.[8] The problem is that the zincate ions are soluble in an aqueous alkaline electrolyte. When the zincate ions are formed, the ions detach from the Zn surface and dissolve in the electrolyte. Eventually the Zn particles lose electrical connection rendering the anode no longer rechargeable. As the Zn anode is a promising anode for both alkaline batteries[7,9] and metal–air batteries,[6,10,11] resolving the rechargeability with the Zn anode is beneficial for the field of electrical energy storage.

To overcome this issue, there are numerous reports utilizing various methods including composite addition, electrolyte modification, and nanostructuring.[12–16] Among them, the composite addition of Bi_2O_3 is notable for its simplicity and effectiveness. Some reports show that Bi_2O_3 significantly improves the cycling performance of the Zn anode; however much of the literature suggests that enhanced cycle performance is due to advanced electrical conductivity.[16,17] Moser *et al.* observed Bi metal formation through *in situ* powder X-ray diffraction (PXRD) and concluded that the Bi metal further increased the conductivity.[17] However, it is difficult to argue that Bi_2O_3 is the most effective additive to elevate the electrical conductivity. Bi_2O_3 exhibits p-type electronic conductivity at room temperature, but it is heavy and not easy to obtain a high surface area.[18] Using Bi_2O_3 as a conductive additive makes the whole electrode too heavy without providing much electrical connection. A more optimum choice to increase the conductivity

University of California San Diego, NanoEngineering Department, 9500 Gilman Dr., (MC:0448), La Jolla, CA92093, USA. E-mail: shmeng@ucsd.edu, josephwang@ucsd.edu; Fax: +1-8585349553; Tel: +1-8588224247

† Electronic supplementary information (ESI) available. See DOI: 10.1039/c6cp04566a

‡ These authors contributed equally to this work.

is to employ simple conductive carbon with a high surface area. But it is known that the benefit of Bi_2O_3 surpasses that of the carbon.[19] Therefore, a more comprehensive understanding of the mechanism of a Zn and Bi_2O_3 composite electrode is needed. This paper proposes that when the zincate ions are formed, the ions are deposited onto the surface of the bismuth species, which allows the Zn anode to be rechargeable. The authors prove this with various characterizations of the composite electrode at different states of electrochemical cycles.

2. Experimental section

Cell fabrication

All inks were prepared by first preparing the polyvinylidene fluoride (PVDF) solution. PVDF solution is prepared by dissolving 1 g of PVDF (MTI, EQ-Lib-PVDF) in 10 ml of *n*-methyl-2-pyrrolidone (NMP) (MTI EQ-Lib-NMP). The PVDF was dissolved overnight after vortex mixing and sonication. Then the appropriate amount of PVDF solution was added to the composite powder. The mass ratio of the composite powder and PVDF is illustrated in the ESI.† The active electrode area was 0.7 cm × 0.9 cm and the distance between the electrodes was maintained at 2 mm. Electrode patterns were designed in AutoCAD (Autodesk, San Rafael, CA) and outsourced for fabrication on stainless steel through-hole 12 inch framed stencils (Metal Etch Services, San Marcos, CA). A conductive carbon ink (ERCON E3449) was printed as a carbon based current collector layer on a polyethylene terephthalate (PET) film. On the current collector layer, the respective electrodes were printed. The printing was performed by employing an MPM-SPM semiautomatic screen printer (Speedline Technologies, Franklin, MA). For the three-electrode cell electrochemical experiments, the Zn electrode was taped to a glass slide in between two strips of Zn foil (Sigma-Aldrich 356018). The two strips of Zn foils were utilized as the counter electrode and the reference electrode. Then the gel based electrolyte was prepared with polyacrylic acid.[20] The electrolyte was extruded onto the three-electrodes *via* a syringe.

Electrochemical tests

The electrochemical tests were conducted using Arbin electrochemical cycler channels. All the electrochemical cycling tests were conducted with galvanostatic discharge at a current density of 4 mA cm^{-2} and constant current constant voltage charge at a current density of 2 mA cm^{-2} and constant voltage hold for 20 min at −0.3 V *vs.* Zn/Zn^{2+} for three-electrode cells and 2.05 V *vs.* Zn/Zn^{2+} for a full-cell. The three-electrode cells were cycled in the −0.3–0.4 V Zn/Zn^{2+} range and the full-cell was cycled in the 0.8–2.05 V Zn/Zn^{2+} range. The three-electrode cells were cycled with a capacity limit of 1 mA h cm^{-2}.

PXRD

The pristine sample is the Zn + Bi_2O_3 electrode. The soaked sample is the pristine sample soaked in the electrolyte for the same time as oxidized sample (45 minutes). The oxidized sample is the pristine sample after electrochemical oxidation (discharge). Both the soaked sample and the oxidized sample were washed with running D.I. water and soaked in the D.I. water overnight. After washing, the electrode was dried in 60 °C for 3 hours. All the PXRD data were collected at an ambient temperature on a Bruker D8 Advance diffractometer at 40 kV, 40 mA for Cu K_α (λ = 1.5418 Å), with a scan speed of 1 s per step, a step size of 0.05° in 2θ, and a 2θ range of ~10–80°.

Raman spectroscopy

The Raman samples were prepared in the same way as the PXRD samples. The Raman spectra were recorded using a Renishaw InVia Raman microscope, with a laser excitation source of 514 nm, a magnification of 20×, a power of 0.1%, and three accumulations of 30 seconds. For the oxidized sample, ten different spots were examined to confirm the consistent results.

Scanning electron microscopy/energy dispersive X-ray spectroscopy (SEM/EDS)

The SEM/EDX samples were prepared in the same way as the PXRD samples. After drying, the electrodes were scraped off from the PET substrate and ground in an agate mortar and pestle. The electrode powder was then loaded onto a SEM holder using a carbon adhesive tape. The images and the EDS mapping were obtained using a 10 kV energy source using the FEI/Phillips XL30 ESEM.

X-ray photoelectron spectroscopy (XPS)

The electrode samples were prepared in the same way as the PXRD samples. Then the electrodes were adhered to a Si wafer using carbon tape. The baseline powders were also adhered to a Si wafer using carbon tape. XPS was performed using a Kratos AXIS Supra with the Al anode source operated at 15 kV. The chamber pressure was $<10^{-8}$ Torr during all measurements. High resolution spectra were calibrated using the hydrocarbon C1s peak at 284.8 eV. Fitting was performed using CasaXPS software using a Shirley-type background.

3. Results

The three-electrode system of various Zn cells is electrochemically cycled (Fig. 1). When the electrode only contains Zn, the cell cycles only 8 times with a small capacity, followed by a rapid capacity failure. With the addition of Super-P (SP), a conductive carbon additive, the capacity retention exponentially decays in the first ten cycles, gradually decreases until 40 cycles, and finally has no capacity after 50 cycles. By including ZnO, the electrode cycles only two times with zero capacity output. When added with Bi_2O_3, the capacity exponentially decays for the first three cycles but increases back to 1 mA h cm^{-2} over the next 12 cycles. This Zn electrode with the Bi_2O_3 additive is referred to as the Bi_2O_3 electrode. With the addition of all three additives, the capacity remains at 1 mA h cm^{-2} for at least 50 cycles. Bi_2O_3, compared to SP, increases in capacity after the exponential decay and after 15 cycles, the capacity

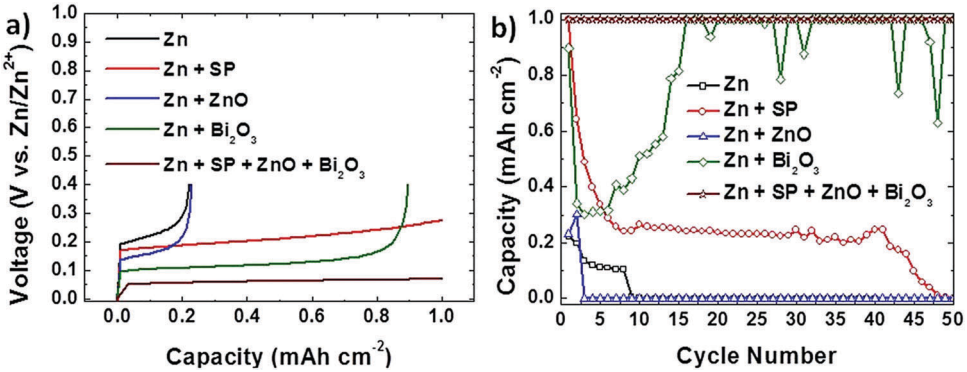

Fig. 1 (a) First discharge voltage profile and (b) discharge cycle retention of various Zn electrode electrochemically cycled in a three-electrode cell. All electrodes contain PVDF as the polymer binder but PVDF is omitted for clarity. All electrodes are cycled at a current density of 4 mA cm^{-2} and a capacity limit of 1 mA h cm^{-2}.

retention stays mostly at 1 mA h cm^{-2}. Although adding all three additives improves the capacity retention, it is worthwhile to understand the role of Bi_2O_3 to form strategies to further enhance the rechargeability.

Since the Zn oxidizes to form ZnO crystals, PXRD of the Bi_2O_3 electrode is obtained at various states (Fig. 2a). In the pristine electrode, there are clear reflections from both Zn metal and Bi_2O_3. After being soaked in the electrolyte, the Bi_2O_3 reflections disappear, but reflections corresponding to Bi metal appear. To confirm the absence of Bi_2O_3 reflections, the same mass amount of Zn and Bi_2O_3 is mixed and soaked in the electrolyte. It shows the absence of Bi_2O_3 and Bi metal-like reflections (Fig. S1, ESI†). The Bi_2O_3 is reduced without electrochemical bias. The Zn and Bi_2O_3 particles separately in the electrolyte do not form a new crystal phase (Fig. S2, ESI†). A new phase is only formed when Zn is present with the Bi_2O_3 in the electrolyte.

After 50 cycles, the ZnO reflections become obvious but the Zn and Bi metal-like reflections vanish. This suggests that the Bi metal-like species is actively involved during the electrochemical cycling; however the ZnO growth is not very clear upon first oxidation. To elucidate the electrochemical reaction that occurs in the Bi_2O_3 electrode, Raman spectra are obtained before and after the electrochemical oxidation reaction (Fig. 2b). Before the electrochemical reaction, the pristine electrode only shows the typical Bi_2O_3 vibration modes. Upon oxidation reaction, the Bi_2O_3 vibration modes disappear, similar to the Bi_2O_3 reflections in PXRD, and only two broad peaks appear near 440 cm^{-1} (E_2 (high) mode) and 565 cm^{-1} (A_1 (longitudinal optical or LO) mode). These two peaks indicate ZnO formation. The E_2 (high) mode is typically an intense and sharp signal originated from the vibrational motion of oxygen atoms in ZnO.[21] The low intensity and the broadening imply a disorder in the crystal structure.[21,22] The disorder can be a result of lattice mismatch from relaxation, reconstruction, structural imperfection, and adsorbed impurities.[23] A_1 (LO) mode is typically a low intensity signal from c-face ZnO. The enhancement of this signal is due to the Raman resonance effect.[24] The observed resonance effect is most likely due to ZnO that is not nucleated as an isolated compound but rather deposited on a conductive substrate/surface. The Raman signal may be contributed by the passivation ZnO layer on the Zn metal or on the Bi metal-like species. Further experiments are conducted to identify the exact location of ZnO.

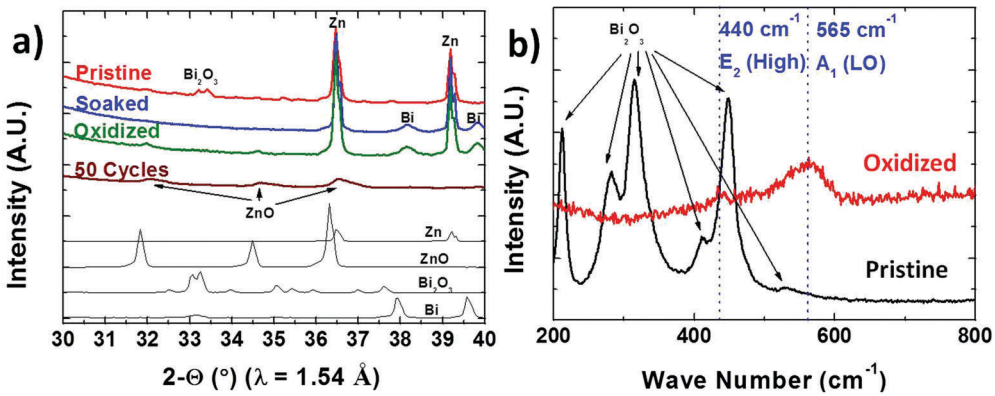

Fig. 2 (a) PXRD of the Bi_2O_3 electrode at various states in color and raw materials in black. (b) Raman spectra of the Bi_2O_3 electrode at pristine and oxidized (first discharged). The pristine sample is the Bi_2O_3 electrode after curing. The soaked sample is the Bi_2O_3 electrode after soaking in the electrolyte. The oxidized sample is the Bi_2O_3 electrode after first electrochemical oxidation or discharge.

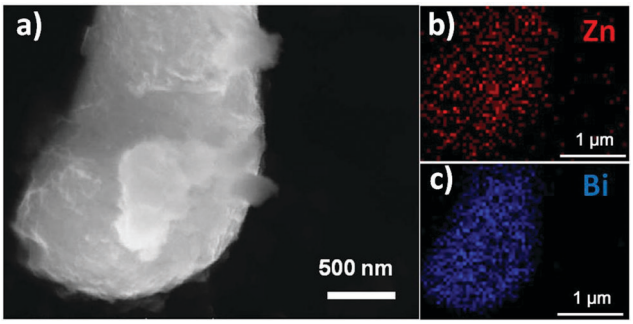

Fig. 3 (a) SEM image of the bismuth species after oxidation. (b) EDS mapping of Zn $K\alpha_1$ and (c) Bi $M\alpha_1$. The EDS mapping is performed on the same particle as the SEM image (a).

The Raman spectra suggest that the ZnO is formed on a conductive surface, yet it is not clear whether the ZnO observed in Raman is a passivation layer on the Zn metal or on the surface of the bismuth species. SEM images along with the EDS mapping are collected after oxidation. Pristine Bi_2O_3 particles are about 2 μm in size. EDS mapping of a 2 μm particle shows that this particle is composed of both zinc and bismuth atoms (Fig. 3). This mapping suggests that the ZnO is deposited on the surface of the bismuth species. Furthermore, the EDS mapping of a particle after 50 cycles also exhibits both Zn and Bi (Fig. S3, ESI†). Unlike after the first oxidation, this particle is about 8 μm and the concentration of Zn is much higher than that of Bi. The growth of the particle size and the change in atomic concentration clearly indicate that the ZnO continues to grow on the surface of the bismuth species over prolonged cycles. Without the electrochemical bias, both Bi_2O_3 and Bi metal are soaked in a 6 M $Zn(NO_3)_2$ solution (Fig. S4, ESI†). A clear change in the surface morphology is found, which supports that the deposition of Zn^{2+} ions onto the surface of the bismuth species occurs due to thermodynamic reasons rather than the electrochemical side reaction.

To confirm the ZnO deposition on the bismuth species, XPS is collected for the pristine, electrolyte soaked, and oxidized electrode. The survey scans are provided to ensure the absence of electrolyte salts or other impurities (Fig. S5, ESI†). The pristine electrode contains the Zn metal and Bi_2O_3 with respective surface passivation layers (Fig. 4).[25–27] After being soaked in the electrolyte, the Zn metal peak shifts to lower binding energy indicative of the Zn alloying.[28] In the Bi 4f spectra, the Bi_2O_5 passivation layer disappears and the Bi metal peak appears. The absence of Bi_2O_5 and the presence of the Bi metal support the hypothesis that Zn reduces the bismuth species. Furthermore, compared to the Bi metal baseline spectrum, the spectrum of the soaked sample is much broader. This is likely due to Bi–Zn alloying.

Upon oxidation, the Zn alloy peak disappears and the zincate peak appears. This suggests that the alloyed Zn is electrochemically active to form the zincate ion. As mentioned earlier, the zincate ion is soluble in the aqueous electrolyte. Thus the formation of the zincate ion leads the active material loss because the ZnO is developed in the electrolyte disconnected from the electrode. However, the presence of a zincate peak implies that the zincate ion is well bound to the electrode even

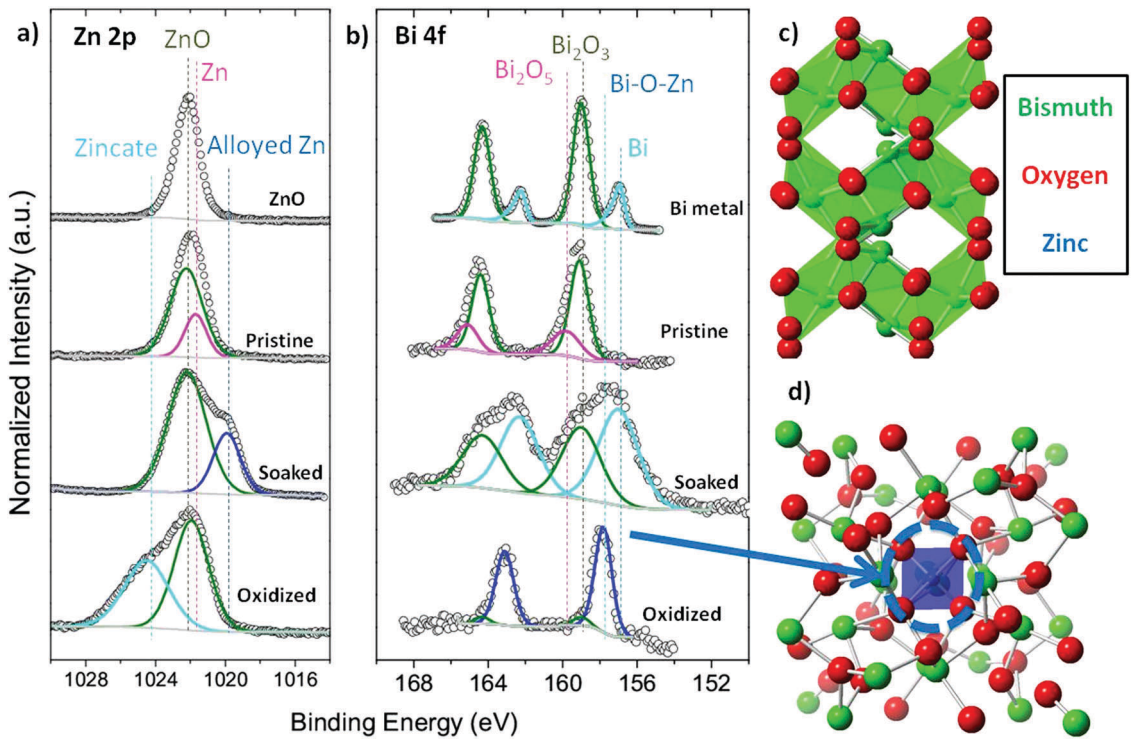

Fig. 4 (a) Zn 2p and (b) Bi 4f XPS of the Bi_2O_3 electrode at various states along with ZnO and Bi metal as baseline materials. Crystal structure of (c) α-Bi_2O_3 and (d) $Bi_{38}ZnO_{58}$. Green: bismuth, red: oxygen, and blue: zinc. In (d) $Bi_{38}ZnO_{58}$, the Zn site is partially occupied by Zn and Bi.

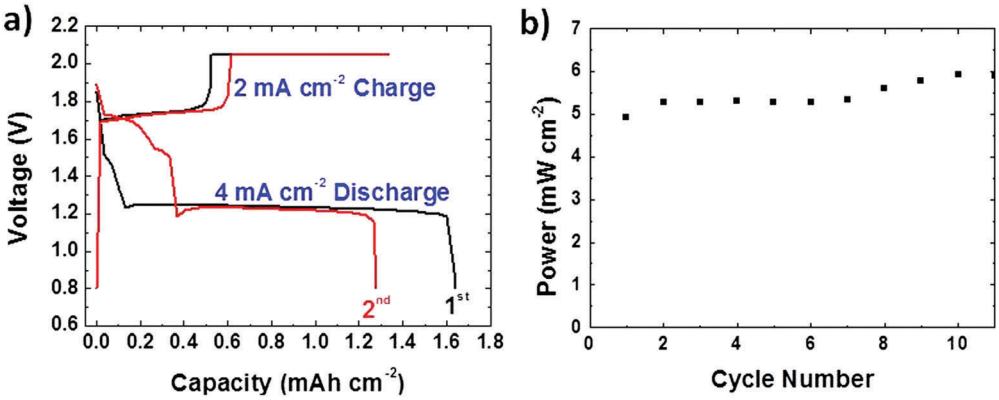

Fig. 5 (a) Voltage profile and (b) power density of Zn–Ag full-cell battery performance with all the additives added in the Zn anode. The full-cell is cycled at a current density of 4 mA cm^{-2} without a capacity limit.

after the rigorous washing. In the Bi 4f spectra, upon oxidation, the Bi metal peak disappears and a new peak appears in between the Bi_2O_3 and Bi metal peaks. Since the Bi^{2+} ion is unstable and undergoes disproportionation reaction, this new peak most likely originates from some Bi^{3+}/Zn^{2+} compounds.[29]

It is clear that Bi_2O_3 provides the vital assistance in prolonging the cyclability of the Zn anode. However, the Bi_2O_3 added electrode suffers from a rapid decay in the retention during the first few cycles. By adding the three additives (Bi_2O_3, SP and ZnO), the cycling performance of the three-electrode cell noticeably improves (Fig. 1b). ZnO is required to match the extra charging capacity of the Ag_2O cathode.[20] Using this anode, a Zn–Ag full-cell is constructed (Fig. 5). The Zn anode behaves as the Zn/Zn^{2+} redox couple and the Ag cathode behaves as the AgO/Ag_2O and Ag_2O/Ag redox couples. There are largely two plateaus in both charge and discharge corresponding to these two redox couples. First discharge curve dominantly consists of Ag_2O/Ag redox behavior because at the beginning, the Ag electrode mostly contains Ag_2O. The full-cell is fully functional even with a high discharge current of 4 mA cm^{-2}. To the best of our knowledge, among Zn-based printable batteries, 4 mA cm^{-2} of discharge current density in this work is among the highest[20,30–35] and for printable batteries, the highest current density to date is 1.4 mA cm^{-2}.[20] During discharge, a consistent high power output of about 5 mW cm^{-2} is achieved. The capacity of the full-cell is above 1.2 mA h cm^{-2} (Fig. 5a). Gaikwad *et al.* achieved about 3.5 mA h cm^{-2}, but their battery is not rechargeable.[30] Among the rechargeable printable batteries, the highest capacity is 1.2 mA h cm^{-2}.[20] Although the cycling retention degrades only after 6 cycles, this is attributed to the decay in the cathode (Fig. S6, ESI†). The bare Zn anode's poor cycling performance originates from the large crystal transformation during the electrochemical reaction and the Ag cathode also undergoes a significant crystal transformation.[20]

4. Discussion

The Zn particles are conductive themselves, yet when Zn starts to oxidize, the Zn surface gets etched away, losing the electrical connections and eventually no capacity is observed, as shown in Fig. 1. A conductive additive is needed even though the Zn particles are conductive. Utilizing Zn plates bypasses such issues; however, Zn plates suffer from dendritic deposition of ZnO.[36] It is reported that the composite electrodes exhibit higher energy density due to their higher surface area and porosity compared to those of the plates.[37,38] Both SP and Bi_2O_3 are conductive additives and they provide electrical connection. Compared to Bi_2O_3, the SP electrode decays in capacity more slowly. This is attributable to the fact that SP has much greater surface area than Bi_2O_3, making it capable of maintaining a better network of electrical connections. However, the SP electrode eventually uses up the electrical network and does not show any capacity. The Bi_2O_3 electrode has low retention between the first cycle and the 15th cycle. Given the high rate cycling, the low retention of the Bi_2O_3 electrode is most likely due to the delay in the relaxation of zincate ions into ZnO. Lastly, the ZnO additive is insulating. Although it helps giving extra capacity at the second cycle by reducing to Zn metal during the first reduction/charge, it does not allow stable electrical conductivity.

The PXRD and XPS results suggest the reduction of Bi_2O_3 into a Zn–Bi alloy. Although Zn is kinetically stable in the aqueous electrolyte, it is not thermodynamically stable because Zn has a lower reduction potential compared to hydrogen. The Zn anode in the aqueous electrolyte oxidizes, which is called self-discharge.[39,40] Self-discharging can be suppressed by the presence of bismuth species.[39,40] Besides the hydrogen, Bi^{3+} also has higher reduction potential than Zn. The Bi^{3+} reduces to form Bi^{2+} or Bi metal to oxidize Zn and after reducing to Bi^{2+}, the Bi^{2+} undergoes disproportionation reaction to form Bi metal.[29] Bi metal-like reflections have been observed and reported in the literature.[17]

In the XPS results, a Bi^{3+}/Zn^{2+} mixed phase is found. At the room temperature, the monoclinic α-Bi_2O_3 phase is stable and all the Bi^{3+} coordination environments are distorted half-octahedron: $[BiO_5E]$ (E denotes an unshared electron pair). At higher temperature, a body-centered cubic (BCC) γ-Bi_2O_3 is the stable phase and some Bi^{3+} coordination environments are tetrahedron: $[BiO_4]$.[41] Furthermore, in the presence of Zn^{2+}, the BCC phase is stable at the room temperature.[41–43]

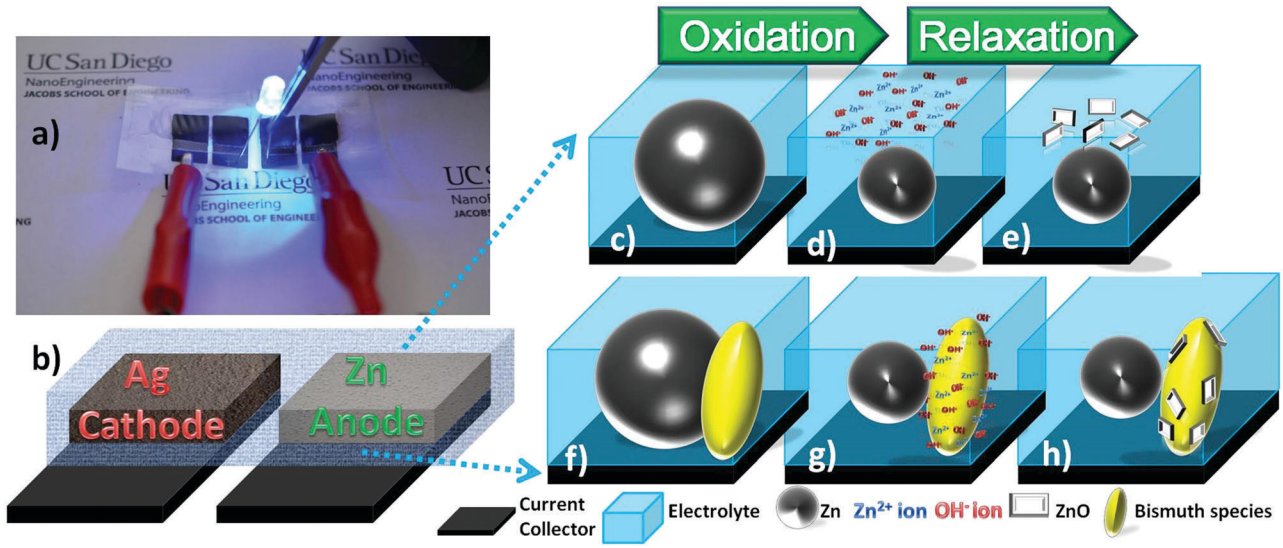

Fig. 6 (a) Two Zn–Ag full-cells lighting up an LED. (b) A conceptual image illustrating the full-cell configuration. Schematics illustrating possible reaction mechanisms for the Zn electrode (c–e) and the Zn with the Bi_2O_3 additive electrode (f–h). In the scheme, the phase transformation of bismuth species, PVDF polymer binder, and polyurethane sealing are omitted for clarity.

$Bi_{38}ZnO_{58}$, part of the sillenite family, is a BCC phase with the tetrahedron coordination environment. Although it is hard to conclude that $Bi_{38}ZnO_{58}$ is formed, we can be certain that a new phase with $[BiO_4]$ local bonding has formed.

The improvement of the rechargeability of the Bi_2O_3 electrode over time is related to the deposition of ZnO rather than conductivity. While this work describes various bismuth species involved during the cycling process, the zincate ions deposit on the surface of the bismuth species regardless of the bismuth species (Fig. S4, ESI†). Based on the findings of this study, a possible reaction mechanism is proposed as shown in Fig. 6. Without the Bi_2O_3 additive, the Zn particles in the electrode upon oxidation form zincate ions. The zincate ions are dissolved in the electrolyte and in ZnO. Since ZnO is not on the electrode where electron pathways are, this electrode is not fully rechargeable. By adding Bi_2O_3, the zincate ions deposit on the surface of the bismuth species and relax into ZnO on the bismuth species, making this electrode rechargeable.

5. Conclusion

Various additives are mixed into the Zn electrodes and their electrochemical performances are presented. Among the additives, Bi_2O_3 is a critical additive for improving the cycle life of the Zn electrode. Through carefully characterizing the Bi_2O_3 containing Zn electrode, we gained the comprehensive mechanistic role of Bi_2O_3. Firstly, upon oxidation, the zincate ions are formed and deposited on the surface of the bismuth species. Secondly, the zincate ions relax into ZnO on the bismuth species. The electrode is fully rechargeable because the electrical connection is retained for the ZnO. Notable additional phenomena were discovered in this work. The Zn–Bi alloy and the new Bi^{3+}/Zn^{2+} mixed oxide phases were found. Although the exact crystal structure of these phases is unknown, the identification of the phases can be achieved through series of computational modeling and experimental investigation. Nevertheless, the benefit of adding Bi_2O_3 is previously assumed to be in conductivity; however this work confirms the vital role of Bi_2O_3 in providing surfaces for the ZnO to deposit. This work clearly defines the mechanistic role of Bi_2O_3 in the Zn electrode. The findings in this work can potentially help gaining a better understanding on the large crystal transformation systems such as conversion systems in LIBs.

Acknowledgements

The information, data, or work presented herein was funded in part by the Advanced Research Projects Agency – Energy (ARPA-E), U.S. Department of Energy, under Award Number DE-AR0000535. This work was performed in part at the San Diego Nanotechnology Infrastructure (SDNI), a member of the National Nanotechnology Coordinated Infrastructure, which is supported by the National Science Foundation (Grant ECCS-1542148). The authors would like to thank Prof. Seth M. Cohen, Prof. Andrea R. Tao, and UC Irvine Materials Research Institute (MRI) (funded in part by the NSF-MRI under grant No. CHE-1338173) for the access to their respective instruments. Lastly, the authors thank P. Y. Meng and T. S. Arnold for assistance in the sample preparation.

References

1 J. P. Deane, B. P. O. Gallachoir and E. J. McKeogh, *Renewable Sustainable Energy Rev.*, 2010, **14**, 1293–1302.
2 J. M. Pearce, *Int. J. Nucl. Governance, Econ. Ecol.*, 2008, **2**, 17.
3 W. Walker, S. Grugeon, O. Mentre, S. Laruelle, J. M. Tarascon and F. Wudl, *J. Am. Chem. Soc.*, 2010, **132**, 6517–6523.

4 W. Walker, S. Grugeon, H. Vezin, S. Laruelle, M. Armand, J. M. Tarascon and F. Wudl, *Electrochem. Commun.*, 2010, **12**, 1348–1351.
5 K. Nakahara, S. Iwasa, M. Satoh, Y. Morioka, J. Iriyama, M. Suguro and E. Hasegawa, *Chem. Phys. Lett.*, 2002, **359**, 351–354.
6 G. Toussaint, P. Stevens, L. Akrour, R. Rouget and F. Fourgeot, *ECS Trans.*, 2010, **28**, 25–34.
7 H. Chen, T. N. Cong, W. Yang, C. Tan, Y. Li and Y. Ding, *Prog. Nat. Sci.*, 2009, **19**, 291–312.
8 H. I. Kim, E. J. Kim, S. J. Kim and H. C. Shin, *J. Appl. Electrochem.*, 2015, **45**, 335–342.
9 M. Minakshi, *Ind. Eng. Chem. Res.*, 2011, **50**, 8792–8795.
10 H. Ma, C. S. Li, Y. Su and J. Chen, *J. Mater. Chem.*, 2007, **17**, 684–691.
11 Q. Li, P. Xu, B. Zhang, H. H. Tsai, J. Wang, H. L. Wang and G. Wu, *Chem. Commun.*, 2013, **49**, 10838–10840.
12 Z. Liu, T. Cui, G. Pulletikurthi, A. Lahiri, T. Carstens, M. Olschewski and F. Endres, *Angew. Chem., Int. Ed.*, 2016, **55**, 2889–2893.
13 J. Mcbreen and E. Gannon, *J. Power Sources*, 1985, **15**, 169–177.
14 J. Mcbreen and E. Gannon, *Electrochim. Acta*, 1981, **26**, 1439–1446.
15 T. J. Simons, M. Salsamendi, P. C. Howlett, M. Forsyth, D. R. MacFarlane and C. Pozo-Gonzalo, *ChemElectroChem*, 2015, **2**, 2071–2078.
16 H. Huang, S. J. Gu, Y. P. Gan, X. Y. Tao and W. K. Zhang, *Advances in Chemical Engineering, Part 3*, 2012, **396–398**, 1725–1729.
17 F. Moser, F. Fourgeot, R. Rouget, O. Crosnier and T. Brousse, *Electrochim. Acta*, 2013, **109**, 110–116.
18 H. A. Harwig and A. G. Gerards, *J. Solid State Chem.*, 1978, **26**, 265–274.
19 H. S. Tao, X. Tong, L. Gan, S. Q. Zhang, X. M. Zhang and X. Liu, *J. Alloys Compd.*, 2016, **658**, 119–124.
20 S. Berchmans, A. J. Bandodkar, W. Z. Jia, J. Ramirez, Y. S. Meng and J. Wang, *J. Mater. Chem. A*, 2014, **2**, 15788–15795.
21 A. Peles, V. P. Pavlovic, S. Filipovic, N. Obradovic, L. Mancic, J. Krstic, M. Mitric, B. Vlahovic, G. Rasic, D. Kosanovic and V. B. Pavlovic, *J. Alloys Compd.*, 2015, **648**, 971–979.
22 H. F. Liu, S. Tripathy, G. X. Hu and H. Gong, *J. Appl. Phys*, 2009, **105**, 053507.
23 *Surface Physics*, ed. M. Prutton, Oxford University Press, Thetford, 1983.
24 J. W. Tringe, H. W. Levie, S. K. McCall, N. E. Teslich, M. A. Wall, C. A. Orme and M. J. Matthews, *Appl. Phys. A: Mater. Sci. Process.*, 2012, **109**, 15–23.
25 A. Nakata, H. Arai, T. Yamane, T. Hirai and Z. Ogumi, *J. Electrochem. Soc.*, 2016, **163**, A50–A56.
26 H. Y. Fan, G. N. Wang and L. L. Hu, *Solid State Sci.*, 2009, **11**, 2065–2070.
27 N. B. Tahar and A. Savall, *J. Appl. Electrochem.*, 1999, **29**, 277–283.
28 X. J. Wang, N. Liu, S. Shi and Y. X. Chen, *Adv. Mater. Sci. Eng.*, 2015, **2015**, 257231.
29 T. A. Hanna, A. L. Rieger, P. H. Rieger and X. Y. Wang, *Inorg. Chem.*, 2002, **41**, 3590–3592.
30 A. M. Gaikwad, A. M. Zamarayeva, J. Rousseau, H. W. Chu, I. Derin and D. A. Steingart, *Adv. Mater.*, 2012, **24**, 5071–5076.
31 G. Kettlgruber, M. Kaltenbrunner, C. M. Siket, R. Moser, I. M. Graz, R. Schwodiauer and S. Bauer, *J. Mater. Chem. A*, 2013, **1**, 5505–5508.
32 C. Y. Yan, X. Wang, M. Q. Cui, J. X. Wang, W. B. Kang, C. Y. Foo and P. S. Lee, *Adv. Energy Mater.*, 2014, **4**, 1301396.
33 R. Winslow, C. H. Wu, Z. Wang, B. Kim, M. Keif, J. Evans and P. Wright, *J. Phys.: Conf. Ser.*, 2013, **476**, 012085.
34 T. Tsukamoto and S. Tanaka, *15th International Conference on Micro and Nanotechnology for Power Generation and Energy Conversion Applications* (*Powermems 2015*), 2015, 660.
35 K. T. Braam, S. K. Volkman and V. Subramanian, *J. Power Sources*, 2012, **199**, 367–372.
36 T. Gupta, A. Kim, S. Phadke, S. Biswas, T. Luong, B. J. Hertzberg, M. Chamoun, K. Evans-Lutterodt and D. A. Steingart, *J. Power Sources*, 2016, **305**, 22–29.
37 M. Minakshi and M. Ionescu, *Int. J. Hydrogen Energy*, 2010, **35**, 7618–7622.
38 M. Minakshi, D. Appadoo and D. E. Martin, *Electrochem. Solid-State Lett.*, 2010, **13**, A77–A80.
39 S. M. Lee, Y. J. Kim, S. W. Eom, N. S. Choi, K. W. Kim and S. B. Cho, *J. Power Sources*, 2013, **227**, 177–184.
40 M. Yano, S. Fujitani, K. Nishio, Y. Akai and M. Kurimura, *J. Power Sources*, 1998, **74**, 129–134.
41 J. P. Guha, S. Kune and D. Suvorov, *J. Mater. Sci.*, 2004, **39**, 911–918.
42 S. F. Radaev and V. I. Simonov, *Kristallografiya*, 1992, **37**, 914–941.
43 T. I. Mel'nikova, G. M. Kuz'micheva, N. B. Bolotina, V. B. Rybakov, Y. V. Zubavichus, N. V. Sadovskaya and E. A. Mar'ina, *Crystallogr. Rep.*, 2014, **59**, 353–361.

